

Reduced Order Modeling of Nonlinear Dynamical Systems Using Slow Manifolds

Dan Wilson ^{*1}

¹Department of Electrical Engineering and Computer Science, University of Tennessee,
Knoxville, TN 37996, USA

July 17, 2025

Abstract

Model order reduction in high-dimensional, nonlinear dynamical systems is often enabled through fast-slow timescale separation. One such approach involves identifying a low-dimensional slow manifold to which the state rapidly converges and subsequently studying the behavior on the slow manifold. Leveraging the isostable coordinate framework, which considers the slowest decaying principle Koopman eigenmodes of a stable attractor, this work investigates the relationships between stable and unstable fixed points and periodic orbits and associated slow manifolds embedded in state space. It is found that under appropriate technical conditions, a slow manifold is formed by the intersection of the unstable manifold of an unstable fixed point (resp., periodic orbit) and the stable manifold of a stable periodic orbit (resp., fixed point). This insight allows for the straightforward computation of slow manifolds that enable model order reduction. Detailed examples are provided for two different highly nonlinear dynamical systems, the first being a coupled system of Hodgkin-Huxley neurons and the second being a biophysically detailed model of circadian oscillations. The resulting reduced order models are illustrated in the consideration of two different biologically motivated control objectives.

1 Introduction

High dimensionality is a common factor that precludes mathematical analysis and control design in many nonnegligibly nonlinear dynamical systems necessitating the use of model order reduction algorithms as a preliminary step in the analysis. Model order reduction of nonlinear dynamical systems is often enabled by exploiting an inherent timescale separation between the fast and slow dynamics. For instance, center manifold theory [32] can be applied in certain situations (and is particularly useful for bifurcation analysis). In a similar manner, inertial manifolds [7], [6] can be used to define invariant manifolds for dynamical systems that attract solutions exponentially quickly. Singular perturbation theory can be applied when separating fast variables from slow variables to understand how the dynamical behavior evolves on a slow manifold [5], [15] [4], [9]. The dimension of linear models that capture the dynamics near a stable fixed point can be reduced by first diagonalizing the system and truncating all rapidly decaying eigenmodes, as gauged by the real component of the associated eigenvalues. This approach can be extended to nonlinear

^{*}corresponding author: dwilso81@utk.edu

dynamical systems using spectral submanifolds [10], [28], [3] which are often approximated through asymptotic expansion.

This work focuses on the use of isostable coordinates to define and study dynamical behavior that is characterized by timescale separation between fast and slow dynamics. Isostable coordinates can be formally defined as the principal Koopman eigenmodes [24], [17] associated with either a stable fixed point or a periodic orbit. For instance, considering a general dynamical system

$$\dot{x} = F(x), \quad (1)$$

with $x \in \mathbb{R}^N$, letting x_0 be a fixed point with $\lambda_1, \dots, \lambda_N$ being eigenvalues associated with its linearization, for any solution $x(t)$ that satisfies (1), the isostable coordinates ψ_1, \dots, ψ_N evolve in time according to

$$\frac{d\psi_j(x(t))}{dt} = \lambda_j \psi_j, \quad (2)$$

for $j = 1, \dots, N$ [34], [38]. Ordering the isostable coordinates in terms of their decay rate so that $|\text{Real}(\lambda_k)| \leq |\text{Real}(\lambda_{k+1})|$, provided there is some separation between the real components of the eigenvalues, a small subset of the slowest decaying isostable coordinates can be used to define a reduced order coordinate system [21], [41], [40] that can subsequently be used for mathematical analysis and control design [37], [1], [27].

Many Koopman-based approaches such as dynamic mode decomposition (DMD) [29], [33], [16] or strategies that seek to identify Koopman invariant subspaces [2], [19], [14] attempt to provide an approximate linear representation of a nonlinear dynamical system using a lifted coordinate basis. Isostable-coordinate-based methods differ from these approaches in that they retain the essential nonlinear characteristics of the underlying system, providing a coordinate system that isolates the slow dynamics. Indeed, using isostable coordinates it is straightforward to define a slow manifold:

$$S = \{x \in \mathbb{R}^N | \psi_k(x) = 0 \text{ for } k > \beta\}. \quad (3)$$

Provided there is a large enough gap between ψ_β and $\psi_{\beta+1}$, solutions rapidly converge to the slow manifold so that the dynamics of the full, nonlinear system can be well approximated by considering the dynamics on S . While (3) provides a relatively simple definition of a slow manifold, numerical challenges associated with the separation between fast and slow timescales often make computation of S challenging. Previous work has focused on strategies that compute an asymptotic expansion of the slow manifold in a close neighborhood of a fixed point [38], [20] or a periodic orbit [40], [35]. These approaches, however, are typically insufficient for use with model order reduction when large magnitude inputs are required and the computational complexity of these approaches makes them difficult to implement in high dimensional systems. Recent work [36] investigated strategies for computation of trajectories in backward time along the slow manifold, but these methods were difficult to implement when computing the slow manifold far from the underlying stable attractor.

In contrast to previously developed computational methods for the identification of slow manifolds, this work explores the slow manifold in relation to the stable/unstable fixed points and periodic orbits of the underlying dynamical system (1). As a concrete example, consider a 3-dimensional toy model

$$\begin{aligned} \dot{\phi} &= 1 + r^2, \\ \dot{r} &= k_1 r (0.5r^2 - 1), \\ \dot{z}_3 &= 200z_3(z_3 - r_0)(k_2 r_0 - r). \end{aligned} \quad (4)$$

Here, $k_1 = 1$, $k_2 = 0.9$, $r_0 = \sqrt{2}$, $\phi \in [0, 2\pi)$ and $r \in \mathbb{R}^+$. The ϕ and r dynamics are governed by the Hopf normal form with a transformation $z_1 = r \cos(\phi)$ and $z_2 = r \sin(\phi)$ to Cartesian coordinates.

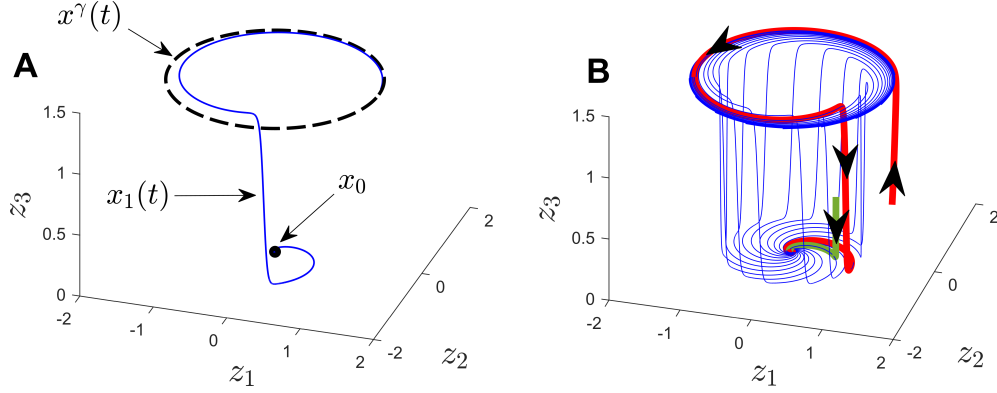


Figure 1: Panel A shows a toy system (4) with an unstable periodic orbit (dashed line), stable fixed point (black dot) and trajectory $x_1(t)$ which is on both the stable manifold of x_0 and the unstable manifold of $x^\gamma(t)$. In panel B, blue lines show a collection of trajectories on the intersection of the stable manifold of x_0 and the unstable manifold of $x^\gamma(t)$. Two trajectories in red and green rapidly converge to this manifold on their way to the stable fixed point. Theoretical results from Section 3.1 show that the intersection of these stable and unstable manifolds is indeed a slow manifold of (4).

This model has a stable fixed point x_0 at $z_1 = z_2 = z_3 = 0$ and an unstable periodic orbit $x^\gamma(t)$ at $r = z_3 = \sqrt{2}$. In panel A of Figure 1, the trajectory $x_1(t)$ is on the intersection of stable manifold of the fixed point x_0 and the unstable manifold of x^γ . Panel B illustrates that trajectories are rapidly attracted this 2-dimensional surface.

With the example from Figure 1 in mind, it can be shown that the system (4) has a slow manifold traced by the blue lines in panel B. In general, as shown in this work, one finds that under appropriate technical conditions, the intersection of an unstable manifold of an unstable fixed point (resp., periodic orbit) and the stable manifold of a stable periodic orbit (resp., fixed point) comprises a slow manifold, as defined by (3). This ultimately allows for a straightforward computation of the slow manifold by choosing a family of trajectories on the unstable manifold near the unstable equilibrium and integrating forward in time; the resulting slow manifold can ultimately be used for reduced order modeling purposes. The organization of this paper is as follows: Section 2 provides necessary background information on isostable coordinates of both stable fixed points and periodic orbits. Section 3 gives a derivation of the main theoretical results. Section 4 provides two numerical illustrations, identifying a slow manifold in a coupled system of Hodgkin-Huxley neurons and in a biophysically detailed model for circadian oscillations. In each example, the resulting reduced order model is used to formulate and solve two biologically motivated control objectives. Section 5 provides concluding remarks.

2 Background

2.1 Isostable Coordinates of Fixed Points

Consider a general dynamical system

$$\dot{x} = F(x) + u(t), \quad (5)$$

where $x \in \mathbb{R}^N$, F gives the dynamics, and u is an external input. For the moment, taking $u = 0$, suppose (5) has with a stable fixed point x_0 for which $F(x_0) = 0$. Local linearization yields

$$\Delta \dot{x} = J \Delta x + O(\|\Delta x\|^2), \quad (6)$$

where $\Delta x = x - x_0$ and J is the Jacobian evaluated at x_0 . While (6) is only valid in a close neighborhood of the fixed point, the spectrum of F can be used to define isostable coordinates which correspond to level sets of principal Koopman eigenfunctions [23], [21], [22] and can ultimately be used to characterize the behavior of solutions in the basin of attraction of the fixed point. To do so, let w_k , v_k and λ_k be left eigenvectors, right eigenvectors, and eigenvalues of J , respectively, ordered so that $|\text{Real}(\lambda_k)| \leq |\text{Real}(\lambda_{k+1})|$. Additionally, suppose that the left and right eigenvectors are scaled so that $w_k^T v_k = 1$ where T denotes the transpose. For the slowest decaying eigenvalue, λ_1 , an associated principal isostable coordinate $\psi_1(x)$ can be defined according to

$$\psi_1(x) = \lim_{t \rightarrow \infty} (w_1^T (\phi(t, x) - x_0) \exp(-\lambda_1 t)), \quad (7)$$

where $\phi(t, x)$ denotes the flow of (5) when $u(t) = 0$. Additional isostable coordinates can be defined as level sets of principal Koopman eigenfunctions [17]. When $u(t) = 0$, under the flow of (5) in the basin of attraction of the fixed point, isostable coordinates evolve in time according to

$$\dot{\psi}_j = \lambda_j \psi_j, \quad (8)$$

for $j = 1, \dots, N$. To a linear approximation, the isostable coordinates are equivalent to using an eigenbasis associated with the local linearization, i.e., provided $\psi_k = O(\epsilon)$ where $0 < \epsilon \ll 1$

$$x = x_0 + \sum_{k=1}^{\beta} \psi_k v_k + O(\epsilon^2). \quad (9)$$

As distinct from local linearization, however, as shown in [38], it is possible to extend the approximation (9) to higher orders of accuracy.

2.2 Phase and Isostable Coordinates of Periodic Orbits

Phase and isostable coordinates can also be defined for systems of the form (5) that have a stable T -periodic orbit $x^\gamma(t)$ when $u = 0$. The phase coordinates capture the timing of oscillations while isostable coordinates give a sense of the decay of perturbations transverse to the limit cycle. A phase $\theta \in [0, 2\pi)$ can be assigned for all $x \in x^\gamma$, scaled so that $d\theta/dt = \omega$ for solutions evolving under the flow of (5). Isochrons [42], [8] can be used to define phase in the basin of attraction of x^γ as follows: for some $a(0) \in x^\gamma$, letting $\theta(a(0)) = \theta_1$, the θ_1 level set (i.e., isochron) is defined as the set of all $b(0)$ such that

$$\lim_{t \rightarrow \infty} \|a(t) - b(t)\| = 0, \quad (10)$$

where $\|\cdot\|$ is some vector norm. Isostable coordinates for periodic orbits can also be defined leveraging Floquet theory [13]. Local linearization near the periodic orbit yields

$$\Delta \dot{x} = J(t) \Delta x + O(\|\Delta x\|^2), \quad (11)$$

where $\Delta x = x - x^\gamma(t)$ and $J(t)$ is the Jacobian evaluated at $x^\gamma(t)$. Letting Φ be the fundamental matrix of the linear time-varying system (11) for which $\Delta x(T) = \Phi \Delta x(0)$. For simplicity of

exposition, suppose that Φ is diagonalizable with eigenvalues $\lambda_0, \lambda_1, \dots, \lambda_{N-1}$. Floquet theory allows solutions of (11) to be written as

$$\Delta x(t) = \sum_{j=0}^{N-1} c_j \exp(\kappa_j t) p_j(t) + O(\|\Delta x\|^2), \quad (12)$$

where $\kappa_j = \log(\lambda_j)/T$ are Floquet exponents, $p_j(t)$ are T -periodic Floquet eigenfunctions, and c_j are constants that depend on initial conditions. The Floquet exponents are often sorted so that $\kappa_0 = 0$ (associated with the Floquet multiplier $\lambda_0 = 1$). The remaining Floquet exponents can be sorted according to $\text{Real}(\kappa_j) \geq \text{Real}(\kappa_{j+1})$. Provided x^γ is stable, the slowest decaying isostable coordinate can be defined explicitly according to (cf., [41])

$$\psi_1 = \lim_{k \rightarrow \infty} [q_1^T(t)(x(t) - x^\gamma(t)) \exp(-\kappa_1 t)], \quad (13)$$

where $q_1^T(t)p_1(t) = 1$. Much like the definition (7), which encodes for the slowest decaying eigenmode of a system with a stable fixed point, (13) encodes for the slowest decaying Floquet eigenmode as solutions decay to the stable periodic orbit. Additional isostable coordinates $\psi_2, \dots, \psi_{N-1}$ can be defined as level sets of principal Koopman eigenfunctions [17], [24] of the stable periodic orbit. When $u(t) = 0$, under the flow of (5), in the basin of attraction of the periodic orbit, phase and isostable coordinates evolve in time according to

$$\begin{aligned} \dot{\theta} &= \omega, \\ \dot{\psi}_j &= \kappa_j \psi_j, \end{aligned} \quad (14)$$

for $j = 1, \dots, N-1$. Notice that isostable coordinates have the same unperturbed decay for systems with periodic orbits (8) and for systems with fixed points (14).

2.3 Dynamics of Isostable Coordinates for Fixed Points

Isostable coordinates have previously been used in a wide variety of reduced order modeling applications, [20], [30], [38], [37], [1], [35], [39]. For isostable coordinates defined for both fixed point and periodic orbits, the evolution of the isostable coordinates along solutions $x(t)$ of Equation (5) is

$$\begin{aligned} \frac{d\psi_j}{dt} &= \frac{\partial \psi_j}{\partial x} \frac{dx}{dt} \\ &= I_j^T (F(x) + u(t)) \\ &= \lambda_j \psi_j + I_j^T u(t), \end{aligned} \quad (15)$$

for $k = 1, \dots, N$. Above, $I_j \equiv \frac{\partial \psi_j}{\partial x}$ evaluated at $x(t)$ and the simplification in the third line results from the fact that $\dot{\psi}_j = \lambda_j \psi_j$ when $u = 0$. Along unperturbed trajectories of (5), $I_j(t)$ evolves according to [35],

$$\dot{I}_j = -(J^T - \lambda_j \text{Id}) I_j, \quad (16)$$

for $k = 1, \dots, N$, where J is the Jacobian evaluated at $x(t)$ and Id is an appropriately sized identity matrix. Noting that when $x(t) = x_0$, $\dot{I}_j = 0$ so that Equation (16) simplifies to $0 = (J^T - \lambda_j \text{Id}) I_j$ with solution $I_j = w_j k$. It is often useful to define $g_k \in \mathbb{C}^N$ so that

$$I_j^T g_k = \begin{cases} 1, & \text{if } k = j, \\ 0, & \text{otherwise.} \end{cases} \quad (17)$$

Given the definition (17), it immediately follows that each g_k evolves in time along trajectories $x(t)$ according to the adjoint of (16)

$$\dot{g}_k = (J - \lambda_k \text{Id})g_k. \quad (18)$$

Considering (17) and (8) together, one finds that when $u(t) = 0$,

$$\frac{dx}{dt} = \sum_{j=1}^N \lambda_j \psi_j g_j. \quad (19)$$

2.4 Dynamics of Phase and Isostable Coordinates for Periodic Orbits

The dynamics of phase and isostable coordinates of periodic orbits are almost identical to those of isostable coordinates of fixed points, with the main difference being the inclusion of phase coordinates to encode for the timing of oscillations. Along solutions $x(t)$ of Equation (5), isostable coordinates evolve in time according to

$$\begin{aligned} \frac{d\psi_j}{dt} &= \frac{\partial \psi_j}{\partial x}^T \frac{dx}{dt} \\ &= I_j^T (F(x) + u(t)) \\ &= \kappa_j \psi_j + I_j^T u(t). \end{aligned} \quad (20)$$

Likewise, phase coordinates evolve in time according to

$$\begin{aligned} \frac{d\theta}{dt} &= \frac{\partial \theta}{\partial x}^T \frac{dx}{dt} \\ &= Z^T (F(x) + u(t)) \\ &= \omega + Z^T u(t). \end{aligned} \quad (21)$$

Above, $I_j \equiv \frac{\partial \psi_j}{\partial x}$ and $Z \equiv \frac{\partial \theta}{\partial x}$, both evaluated at $x(t)$. The simplification in the third line results from the fact that $\dot{\psi}_j = \kappa_j \psi_j$ and $\dot{\theta} = \omega$ when $u = 0$. Along unperturbed trajectories of (5), $Z(t)$ and $I_j(t)$ evolve in time according to [38]

$$\begin{aligned} \dot{Z} &= -J^T Z \\ \dot{I}_j &= -(J^T - \kappa_j \text{Id})I_j, \end{aligned} \quad (22)$$

for $j = 1, \dots, N-1$ where J is the Jacobian evaluated at $x(t)$. Above, the evolution equation for the isostable coordinate gradients are identical to those from (16). Similar to the previous section, $g_0, \dots, g_{N-1} \in \mathbb{C}^N$ will be defined as follows: for g_0 ,

$$\begin{aligned} Z^T g_0 &= 1, \\ I_k^T g_0 &= 0, \text{ for all } k, \end{aligned} \quad (23)$$

and for g_1, \dots, g_{N-1} ,

$$\begin{aligned} Z^T g_k &= 0, \\ I_j^T g_k &= \begin{cases} 1, & \text{if } k = j, \\ 0, & \text{otherwise,} \end{cases} \end{aligned} \quad (24)$$

for $k = 1, \dots, N - 1$. Similar to the previous section, each g_k evolves in time along trajectories according to

$$\begin{aligned}\dot{g}_0 &= Jg_0, \\ \dot{g}_k &= (J - \kappa_k \text{Id})g_k,\end{aligned}\tag{25}$$

for $k = 1, \dots, N - 1$. Considering (14) along with (23) and (24), one finds that when $u(t) = 0$,

$$\frac{dx}{dt} = \omega g_0 + \sum_{j=1}^{N-1} \kappa_j \psi_j g_j.\tag{26}$$

3 Slow Manifolds Connecting Unstable Equilibria and Stable Attractors

For systems with either a stable fixed point or a stable periodic orbit, model order reduction is possible when $|\text{Real}(\lambda_\beta)| - |\text{Real}(\lambda_{\beta+1})|$ (or $|\text{Real}(\kappa_\beta)| - |\text{Real}(\kappa_{\beta+1})|$) is large for some β . In these instances, the fast isostable coordinates $\psi_{\beta+1}, \dots, \psi_N$ decay rapidly relative to the slow isostable coordinates so that can be well-approximated by zero and truncated, ultimately yielding a reduced order model. With this in mind, using the isostable coordinate framework, [36] considered the definition of a slow manifold

$$S = \{x \in \mathbb{R}^N | \psi_k(x) = 0 \text{ for } k > \beta\}.\tag{27}$$

Provided there is a large gap between the real components of eigenvalues λ_β and $\lambda_{\beta+1}$, solutions of (5) will converge to S rapidly. The fundamental challenge in implementing this strategy lies in the numerical computation of S . A naive approach would be to consider some initial condition near the fixed point for which $\psi_k(x) = 0$ for $k > \beta$ and integrate backwards in time along the slow manifold. However, strongly attracting directions in forward time become strongly repelling directions in backward time making this approach numerically infeasible. Reference [36] suggested two approaches for computation of S , however, these were only able to provide an approximation of the slow manifold.

Alternatively, consider a general dynamical system with an unstable periodic orbit $x^\gamma(t)$ and a stable fixed point x_0 . Let $W_{x^\gamma}^u$ be the unstable manifold of x^γ and $W_{x_0}^s$ be the stable manifold of x_0 . As shown in Section 3.1, under appropriate technical conditions,

$$W_{x^\gamma}^u \cap W_{x_0}^s \subseteq S,\tag{28}$$

With Equation (28) in mind, one can approximate $W_{x^\gamma}^u$ near $x^\gamma(t)$ through local linearization and simply compute the rest of the trajectory along the slow manifold using forward time integration. This slow manifold can subsequently be used to understand the dynamics of (5) in a reduced order setting. Likewise, as shown in Section 3.3, for a system (5) with an unstable fixed point and a stable periodic orbit,

$$W_{x^\gamma}^s \cap W_{x_0}^u \subseteq S,\tag{29}$$

where $W_{x^\gamma}^s$ is the stable manifold of x^γ and $W_{x_0}^u$ is the unstable manifold of x_0 . Once again, from Equation (29), the slow manifold can be computed by obtaining an approximation of $W_{x_0}^u$ near the fixed point and integrating forward in time.

3.1 Theoretical Result Connecting the Unstable Manifold of a Periodic Orbits to the Slow Manifolds of a Stable Fixed Point

Here we provide a proof of (28). To begin, for a general dynamical system of the form (5), let x_0 be a stable fixed point. Suppose also that when $u(t) = 0$, Equation (5) has an unstable T -periodic orbit $x^\gamma(t)$ with one unstable Floquet multiplier. Suppose that $W_{x^\gamma}^u \cap W_{x_0}^s$ is not empty. Define $\Delta x = x - x^\gamma(t)$. When $\Delta x = O(\epsilon)$ where $0 < \epsilon \ll 1$, linearization of (5) about this periodic orbit yields

$$\begin{aligned}\Delta \dot{x} &= J \Delta x \\ &= A(t) \Delta x,\end{aligned}\tag{30}$$

where $A(t) = \frac{\partial F}{\partial x}|_{x^\gamma(t)}$ is periodic in time. Leveraging Floquet theory [13], solutions of (30) near $x^\gamma(t)$ follow

$$\Delta x(t) = \sum_{j=0}^{N-1} c_j \exp(\kappa_j t) p_j(t) + O(\|x(t) - x^\gamma(t)\|^2),\tag{31}$$

where κ_j are Floquet exponents, $p_j(t)$ are the associated Floquet eigenfunctions, and c_j are constants that depend on initial conditions. For simplicity of exposition, the Floquet exponents from (31) are assumed to be unique. Here, $\text{Real}(\kappa_1) > 0$ corresponds to the unstable mode and $\text{Real}(\kappa_j) < 0$ for $j \geq 2$.

Consider some trajectory $x_1(t)$ on the unstable manifold of $x^\gamma(t)$, $W_{x^\gamma}^u$, and on the stable manifold of x_0 , $W_{x_0}^s$ (See Panel A of Figure 1 for example). Along $x = x_1(t)$, suppose that t is sufficiently small so that $\|x(t) - x^\gamma(t)\| = O(\epsilon)$. Equation (31) can be simplified further by noting that $\Delta x(t)$ approaches zeros as time approaches negative infinity, which implies that $c_0 = 0$ and $c_2, c_3, \dots, c_{N-1} = 0$ yielding

$$\Delta x(t) = c_1 \exp(\kappa_1 t) p_1(t) + O(\epsilon^2).\tag{32}$$

Thus,

$$x_1(t) = x^\gamma(t) + c_1 \exp(\kappa_1 t) p_1(t) + O(\epsilon^2),\tag{33}$$

as t approaches negative infinity. It will be useful to rewrite the $O(\epsilon^2)$ terms from (33) in a slightly different manner

$$x_1(t) = x^\gamma(t) + c_1 \exp(\kappa_1 t) p_1(t) + O(\exp(2\kappa_1 t)).\tag{34}$$

Equation (34) follows from the fact that $\exp(\kappa_1 t) = O(\epsilon)$ as t approaches negative infinity so that $O(\epsilon^2) = O(\exp(\kappa_1 t)^2) = O(\exp(2\kappa_1 t))$. Below, it will be shown that when considering the isostable coordinates defined using the fixed point x_0 , for solutions evolving along the trajectory $x_1(t)$, $\psi_j(x_1(t)) = 0$ for at least $N - 2$ isostable coordinates. Consequently, $W_{x^\gamma}^u \cap W_{x_0}^s \subseteq S$ as stated in (28).

Proof By Contradiction that $N - 2$ Isostable Coordinates are Equal to Zero on $x_1(t)$: Towards contradiction, suppose that $\psi_j(x_1(t)) \neq 0$ for $j = 1, 2$ and 3 . Let these isostable coordinates be ordered so that for their associated eigenvalues, $\text{Real}(\lambda_1) \geq \text{Real}(\lambda_2) \geq \text{Real}(\lambda_3)$. From (19)

$$\frac{dx}{dt} = \sum_{j=1}^3 \lambda_j \psi_j g_j.\tag{35}$$

Note here that ψ_j and g_j are functions of time. Taking the time derivative of (34), for t small enough along $x = x_1$, one finds

$$\begin{aligned}\frac{dx}{dt} &= \dot{x}^\gamma(t) + c_1 \exp(\kappa_1 t)(\kappa_1 p_1(t) + \dot{p}_1(t)) + O(\exp(2\kappa_1 t)) \\ &= \dot{x}^\gamma(t) + c_1 \sigma(t) \exp(\kappa_1 t) + O(\exp(2\kappa_1 t)),\end{aligned}\tag{36}$$

where $\sigma(t)$ is defined appropriately. Comparing (35) and (36), each term $\lambda_j \psi_j g_j$ is of the form

$$\lambda_j \psi_j g_j = \tilde{a}_{j,0} \dot{x}^\gamma(t) + \tilde{a}_{j,1} \sigma(t) \exp(\kappa_1 t) + O(\exp(2\kappa_1 t)),\tag{37}$$

where each $\tilde{a}_{j,k}$ is a constant for $j = 1, 2$, and 3 . If this were not the case, the $O(\epsilon)$ terms of the set $\{g_1, g_2, g_3\}$ would not be linearly independent which would invalidate (17). Letting $\psi_j(t) = \psi_j(0) \exp(\lambda_j t)$, Equation (37) can be written as

$$g_j(t) = a_{j,0} \dot{x}^\gamma(t) \exp(-\lambda_j t) + a_{j,1} \sigma(t) \exp((\kappa_1 - \lambda_j)t) + O(\exp((2\kappa_1 - \lambda_j)t)),\tag{38}$$

for $j = 1, 2, 3$ where $a_{j,0}$ and $a_{j,1}$ are constants.

Next, recall from (16) that $\dot{I}_j = -(J^T - \lambda_j \text{Id}) I_j$ along $x_1(t)$. In the limit as time approaches negative infinity, $J = \frac{\partial f}{\partial x}|_{x_1(t)} = A(t) + O(\|x_1(t) - x^\gamma(t)\|) = A(t) + \epsilon B(t) + O(\epsilon^2)$ where $B(t)$ is defined appropriately. Dropping the $O(\epsilon^2)$ terms from the expansion of the Jacobian, along $x_1(t)$,

$$\dot{I}_j = -(A^T(t) + \epsilon B^T(t) - \lambda_j) I_j(t).\tag{39}$$

For the moment, consider instead solutions of

$$\dot{y} = -(A^T(t) + \epsilon B^T(t)) y.\tag{40}$$

Solutions of (40) are related to solutions of (39) through

$$I_j(t) = y(t) \exp(\lambda_j t).\tag{41}$$

Expanding $y(t)$ in powers of ϵ as $y(t) = \frac{1}{\epsilon} y_0(t) + y_1(t) + \epsilon y_2(t)$ and collecting the $O(1/\epsilon)$ terms yields

$$\dot{y}_0 = -A^T(t) y_0.\tag{42}$$

Noticing (42) is the adjoint equation of (30), solutions of $y_0(t)$ follow the general form

$$y_0(t) = \sum_{k=0}^{N-1} \tilde{b}_k \exp(-\kappa_k(t - t_0)) q_k(t),\tag{43}$$

where \tilde{b}_k are constants and $q_k(t)^T p_k(t) = 1$ if $k = j$, and equals 0 otherwise. As such

$$\begin{aligned}y(t) &= \sum_{k=0}^{N-1} \tilde{b}_k \exp(-\kappa_k(t - t_0)) q_k(t) + O(1) \\ &= \sum_{k=0}^{N-1} b_k \exp(-\kappa_k t) q_k(t) + O(1),\end{aligned}\tag{44}$$

where $b_k = O(1/\epsilon)$. Using Equation (41) in conjunction with (44), one finds

$$I_j(t) = \sum_{k=0}^{N-1} b_{j,k} \exp((\lambda_j - \kappa_k)t) q_k(t) + O(\exp(\lambda_j t)),\tag{45}$$

for $j = 1, 2, 3$, where $b_{j,k}$ are constants.

Taking the product of any $g_k(t)$ and $I_j(t)$ defined according to (38) and (45), respectively, yields

$$\begin{aligned}
I_j^T(t)g_m(t) &= \sum_{k=0}^{N-1} b_{j,k} \exp((\lambda_j - \lambda_m - \kappa_k)t) a_{m,0} q_k^T(t) \dot{x}^\gamma(t) \\
&\quad + \sum_{k=0}^{N-1} b_{j,k} \exp((\lambda_j - \lambda_m + \kappa_1 - \kappa_k)t) a_{m,1} q_k^T(t) \sigma(t) \\
&\quad + O(\exp(\lambda_j t) \left[a_{m,0} \dot{x}^\gamma(t) \exp(-\lambda_m t) + a_{m,1} \sigma(t) \exp((\kappa_1 - \lambda_m)t) \right]) \\
&\quad + \left[\sum_{k=0}^{N-1} b_{j,k} \exp((\lambda_j - \kappa_k)t) q_k(t) + O(\exp(\lambda_j t)) \right]^T O(\exp((2\kappa_1 - \lambda_m)t)). \tag{46}
\end{aligned}$$

Focusing for the moment on the final terms of Equation (46)

$$\begin{aligned}
&\left[\sum_{k=0}^{N-1} b_{j,k} \exp((\lambda_j - \kappa_k)t) q_k(t) + O(\exp(\lambda_j t)) \right]^T O(\exp((2\kappa_1 - \lambda_m)t)) \\
&= O(\exp((\lambda_j - \lambda_m + 2\kappa_1 - \kappa_k)t)) + O(\exp((\lambda_j - \lambda_m + 2\kappa_1)t)). \tag{47}
\end{aligned}$$

Since κ_1 is the largest Floquet exponent, provided $\text{Real}(\lambda_j) \geq \text{Real}(\lambda_m)$, the terms of (47) can be made arbitrarily small in the limit as t approaches negative infinity. With this in mind, and recalling the ordering of the isostable coordinates so that $\text{Real}(\lambda_1) \geq \text{Real}(\lambda_2) \geq \text{Real}(\lambda_3)$, for all $j \leq m$

$$\left[\sum_{k=0}^{N-1} b_{j,k} \exp((\lambda_j - \kappa_k)t) q_k(t) + O(\exp(\lambda_j t)) \right]^T O(\exp((2\kappa_1 - \lambda_m)t)) = O(\epsilon_1), \tag{48}$$

when t is close enough to negative infinity, where $0 < \epsilon_1 \ll 1$.

Finally, from (17)

$$\begin{bmatrix} I_1(t) & I_2(t) & I_3(t) \end{bmatrix}^T \begin{bmatrix} g_1(t) & g_2(t) & g_3(t) \end{bmatrix} = \text{Id}, \tag{49}$$

where $\text{Id} \in \mathbb{R}^{3 \times 3}$ is the identity matrix. Let

$$\tilde{g}_j(t) = a_{j,0} \dot{x}^\gamma(t) \exp(-\lambda_j t) + a_{j,1} \sigma(t) \exp((\kappa_1 - \lambda_j)t), \tag{50}$$

defined so that each $\tilde{g}_j(t)$ contains only up to the $O(\epsilon)$ terms of each $g_j(t)$. For all $j \leq m$, the product of any \tilde{g}_k and $I_j(t)$ is

$$\begin{aligned}
I_j^T(t) \tilde{g}_m(t) &= I_j^T(t) g_m(t) - \left[\sum_{k=0}^{N-1} b_{j,k} \exp((\lambda_j - \kappa_k)t) q_k(t) + O(\exp(\lambda_j t)) \right]^T O(\exp((2\kappa_1 - \lambda_m)t)) \\
&= I_j^T(t) g_m(t) + O(\epsilon_1). \tag{51}
\end{aligned}$$

Above, the first line follows from (46) and the second line follows from (48). Comparing with (49)

$$\begin{bmatrix} I_1(t) & I_2(t) & I_3(t) \end{bmatrix}^T \begin{bmatrix} \tilde{g}_1(t) & \tilde{g}_2(t) & \tilde{g}_3(t) \end{bmatrix} = \begin{bmatrix} 1 & 0 & 0 \\ \xi_1(t) & 1 & 0 \\ \xi_2(t) & \xi_3(t) & 1 \end{bmatrix} + O(\epsilon_1), \tag{52}$$

where $\xi_1(t)$, $\xi_2(t)$, and $\xi_3(t)$ are potentially large. From (50), \tilde{g}_1 , \tilde{g}_2 , and \tilde{g}_3 are spanned by $\{\dot{x}^\gamma(t), \sigma(t)\}$. As such, the left hand side of (49) is at most rank 2 while the right hand side has rank 3. This yields a contradiction which implies that for solutions evolving along the trajectory $x_1(t)$, $\psi_j(x_1(t)) = 0$ for at least $N - 2$ isostable coordinates.

3.2 Slow Manifolds Originating at Unstable Fixed Points and Terminating at Stable Periodic Orbits

Consider a system with a stable periodic orbit, $x^\gamma(t)$, and an unstable fixed point, x_0 . Suppose $W_{x^\gamma}^s \cap W_{x_0}^u$ is not empty. If the unstable fixed point has exactly two complex-conjugate unstable eigenvalues, the intersection of the stable manifold of x^γ and the unstable manifold of x_0 is also a slow manifold, i.e., as stated by Equation (29). As a concrete example, Equation (4) is once again considered, this time taking $k_1 = -1$, $k_2 = 0.4$. This model now has an unstable fixed point at $z_1 = z_2 = z_3 = 0$ and a stable periodic orbit $x^\gamma(t)$ at $r = z_3 = \sqrt{2}$. In panel A of Figure 2, the trajectory $x_1(t)$ is on the stable manifold of the periodic orbit and the unstable manifold of the fixed point. As shown below, this trajectory is on the slow manifold S of $x^\gamma(t)$ defined according to (27) with $\beta = 2$. The 2-dimensional slow manifold can be identified according to $W_{x^\gamma}^s \cap W_{x_0}^u \subseteq S$ as stated in (29). Panel B illustrates the rapid collapse of initial conditions to the slow manifold.

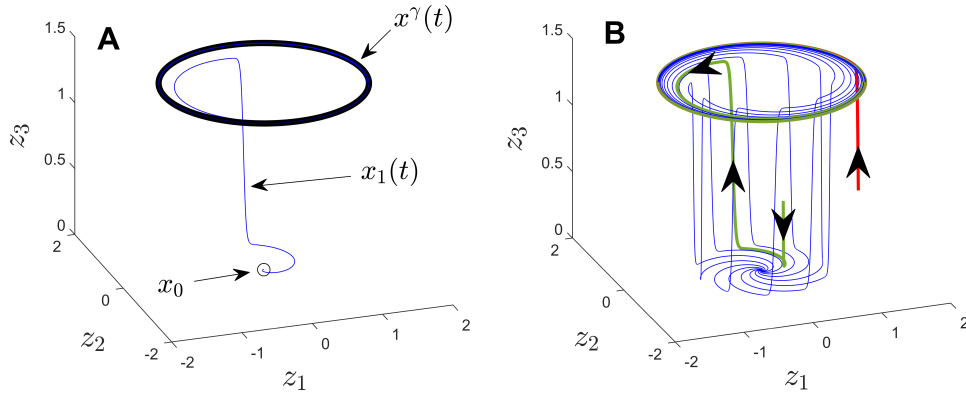


Figure 2: Panel A of the toy system (4) with parameters chosen so that there is an unstable fixed point (black circle) and a stable periodic orbit (solid black line). The trajectory $x_1(t)$ starts on the unstable manifold of x_0 and eventually converges to the periodic orbit, $x^\gamma(t)$. As shown below, $x_1(t)$ is on the slow manifold of x_0 defined according to (27) with $\beta = 2$. In panel B, blue lines show a collection of trajectories on the slow manifold defined according to (29). Two trajectories in red and green rapidly converge to the slow manifold on their way to the stable periodic orbit.

3.3 Theoretical Result Connecting the Unstable Manifold of a Fixed point to the Slow Manifolds of a Stable Periodic Orbit

Suppose that when $u(t) = 0$, Equation (5) has a stable T -periodic orbit $x^\gamma(t)$ as well as an unstable fixed point x_0 . Suppose $W_{x^\gamma}^s \cap W_{x_0}^u$ is not empty. Define $\Delta x = x - x_0$. When $\Delta x = O(\epsilon)$, where $0 < \epsilon \ll 1$, linearization about the periodic orbit yields (6) with solution

$$x = x_0 + \sum_{j=1}^N c_j \exp(\lambda_j t) v_j + O(\|x(t) - x_0\|^2). \quad (53)$$

Above, λ_j are eigenvalues of $A = \frac{\partial F}{\partial x} \Big|_{x_0}$ with corresponding eigenvectors v_j , and c_j are constants. For simplicity of exposition, eigenvalues are assumed to be unique and will be ordered so that $\text{Real}(\lambda_j) \geq \text{Real}(\lambda_{j+1})$. Suppose there are exactly two unstable eigenvalues $\lambda_{1,2} \in \mathbb{C}$ that are complex-conjugates.

Consider some trajectory $x_1(t)$ on the unstable manifold of x_0 , $W_{x_0}^u$, and on the stable manifold of $x^\gamma(t)$, $W_{x^\gamma}^s$ (see Panel A of Figure 2). Along $x = x_1(t)$ when t is sufficiently small, $\|x(t) - x_0\| = O(\epsilon)$. Because the unstable manifold approaches x_0 as t approaches negative infinity, Equation (53) must simplify to

$$\begin{aligned} \Delta x(t) &= \sum_{j=1}^2 c_j \exp(\lambda_j t) v_j + O(\epsilon^2) \\ &= \sum_{j=1}^2 c_j \exp(\lambda_j t) v_j + O(\exp(2\text{Real}(\lambda_1)t)), \end{aligned} \quad (54)$$

Above, the second line follows from the fact that $\exp(\text{Real}(\lambda_1)) = O(\epsilon)$ as t approaches negative infinity so that $O(\epsilon^2) = O(\exp(\text{Real}(\lambda_1))^2) = O(\exp(2\text{Real}(\lambda_1)))$. Below, it will be shown that when considering phase and isostable coordinates defined relative to the periodic orbit $x^\gamma(t)$, for solutions evolving along the trajectory $x_1(t)$, $\psi_j(x_1(t)) = 0$ for all but one isostable coordinate so that $W_{x^\gamma}^s \cap W_{x_0}^u \subseteq S$ as stated in (29). The proof follows the same outline as the one given in Section 3.1, with some minor technical differences resulting from the fact that stability of x_0 and x^γ has been swapped.

Proof By Contradiction that $N-2$ Isostable Coordinates are Equal to Zero on $x_1(t)$: Towards contradiction suppose that for isostable coordinates associated with the stable periodic orbit, $\psi_j(x_1(t)) \neq 0$ for $j = 1$ and 2 . Let these isostable coordinates be ordered so that for their associated Floquet exponents $\text{Real}(\kappa_1) \geq \text{Real}(\kappa_2)$. From (26),

$$\frac{dx}{dt} = \omega g_0 + \sum_{j=1}^2 \kappa_j \psi_j g_j. \quad (55)$$

Taking the time derivative of (54), one finds

$$\frac{dx}{dt} = \sum_{j=1}^2 c_j \lambda_j \exp(\lambda_j t) v_j + O(\exp(2\text{Real}(\lambda_1)t)). \quad (56)$$

Comparing (55) and (56) for t small enough

$$\begin{aligned} \omega g_0 &= \sum_{k=1}^2 \tilde{a}_{0,k} \exp(\lambda_k t) v_k + O(\exp(2\text{Real}(\lambda_1)t)), \\ \lambda_j \psi_j g_j &= \sum_{k=1}^2 \tilde{a}_{j,k} \exp(\lambda_k t) v_k + O(\exp(2\text{Real}(\lambda_1)t)), \end{aligned} \quad (57)$$

for $j = 1, 2$, where each $\tilde{a}_{j,k}$ is a constant. If Equation (57) were not true, the set $\{g_0, g_1, g_2\}$ would not be linearly independent which would invalidate (23) and (24). Letting $\psi_j(t) = \psi_j(0) \exp(\kappa_j t)$, Equation (57) can be rewritten as

$$g_j = \sum_{k=1}^2 a_{j,k} \exp((\lambda_k - \kappa_j)t) v_k + O(\exp((2\text{Real}(\lambda_1) - \kappa_j)t)), \quad (58)$$

for $j = 0, 1, 2$ where $a_{j,k}$ are constants (recall that $\kappa_0 = 0$). Next, recall from (22) that $\dot{Z} = -J^T Z$ and $\dot{I}_j = -(J^T - \kappa_j \text{Id})I_j$ along $x_1(t)$. In the limit as time approaches negative infinity, $J = \frac{\partial f}{\partial x}|_{x_0} = A + O(\|x_1(t) - x^\gamma(t)\|) = A + \epsilon B + O(\epsilon^2)$ where $A, B \in \mathbb{R}^{N \times N}$ are constant matrices. Following a similar set of steps that begins with (39) and ends with (45), one can show that in the limit that t approaches negative infinity along x_1 , Z and I_j can be written as

$$\begin{aligned} Z &= \sum_{k=1}^N b_{0,k} \exp(-\lambda_k t) w_k + O(1), \\ I_j &= \sum_{k=1}^N b_{j,k} \exp((\kappa_j - \lambda_k)t) w_k + O(\exp(\kappa_k t)), \end{aligned} \quad (59)$$

for $k = 1, 2$ where w_1 and w_2 are the left eigenvectors of $A = \frac{\partial f}{\partial x}|_{x_0}$ with corresponding right eigenvectors v_j and the terms $b_{j,k}$ are $O(1/\epsilon)$ constants.

Taking the product of any g_m with both Z and I_j , following a similar set of steps that begins with (46) and ends with (51), one can show that as t approaches negative infinity along x_1 ,

$$\begin{aligned} Z^T g_m &= Z^T \sum_{k=1}^2 a_{m,k} \exp((\lambda_k - \kappa_m)t) v_k + O(\epsilon_1), \\ I_j^T g_m &= I_j^T \sum_{k=1}^2 a_{m,k} \exp((\lambda_k - \kappa_m)t) v_k + O(\epsilon_1), \end{aligned} \quad (60)$$

where $0 < \epsilon_1 \ll 1$ provided $j \leq m$. From Equation (23) and (24),

$$\begin{bmatrix} Z(t) & I_1(t) & I_2(t) \end{bmatrix}^T \begin{bmatrix} g_0(t) & g_1(t) & g_2(t) \end{bmatrix} = \text{Id}. \quad (61)$$

Letting $\tilde{g}_m = \sum_{k=1}^2 a_{m,k} \exp((\lambda_k - \kappa_m)t) v_k$ for $m = 1, 2, 3$ and considering both (61) and (60), one finds

$$\begin{bmatrix} Z(t) & I_1(t) & I_2(t) \end{bmatrix}^T \begin{bmatrix} \tilde{g}_0(t) & \tilde{g}_1(t) & \tilde{g}_2(t) \end{bmatrix} = \begin{bmatrix} 1 & 0 & 0 \\ \xi_1(t) & 1 & 0 \\ \xi_2(t) & \xi_3(t) & 1 \end{bmatrix} + O(\epsilon_1), \quad (62)$$

where (as in Equation (52)) $\xi_1(t), \xi_2(t)$, and $\xi_3(t)$ are potentially large. The vectors \tilde{g}_1, \tilde{g}_2 , and \tilde{g}_3 are spanned by a two-dimensional vector space meaning that the left hand side of (61) can be at most rank 2. Nevertheless, the right hand side has rank 3, yielding a contradiction. As such, for solutions evolving along the trajectory $x_1(t)$, $\psi_j(x_1(t)) = 0$ for at least $N - 2$ isostable coordinates.

4 Reduced Order Modeling in Numerical Examples

Once a slow manifold of the form (27) has been identified, it is possible to use a β -dimensional isostable-coordinate-based reduced order model to approximate full N -dimensional model dynamics (5). Using the results from Section 3 it is generally possible to identify the slow manifold by finding an approximation of the unstable manifold near the unstable fixed point (resp., periodic orbit) and propagating forward in time until it converges to the stable periodic orbit (resp., fixed point). Panel B in Figures 1 and 2 give an illustration of this in a toy model of the form (4). Two numerical illustrations for more substantial models are provided below.

4.1 Maintaining Quiescence in a Model of Coupled Hodgkin-Huxley Neurons

Consider a model of four coupled Hodgkin-Huxley model neurons:

$$C_m \dot{V}_j = -I_{\text{ion}}(V_j, n_j, m_j, h_j) - g_C(V_j - \bar{V}) + B_j + \alpha_j u(t), \quad (63)$$

for $j = 1, \dots, 4$. Here V_j is the transmembrane voltage of neuron j in mV, $I_{\text{ion}}(t)$ is comprised of a set of ionic currents mediated by gating variables n_j , m_j , and h_j , $C_m = 1 \mu\text{F}/\text{cm}^2$ is the membrane capacitance, $B_j = -4.318 + 0.75j \mu\text{A}/\text{cm}^2$ is the baseline current of each neuron, and time is in milliseconds. Coupling is electrotonic [12] with $g_C = 1.5$ and $\bar{V} = \frac{1}{4} \sum_{j=1}^4 V_j$. Here $u(t)$ is an input in the form of a transmembrane current applied to only the first two neurons so that $\alpha_j = 1$ for $j = 1, 2$ and equals zero for $j = 3, 4$. Note that synaptic coupling could also be used instead of electrotonic coupling if desired. A full set of model equations is given in Appendix A. With a total of 4 coupled neurons, each with 4 state variables, this model has a total of 16 state variables.

For the parameters used here, the model (63) is near a subcritical Hopf bifurcation. Panel A of Figure 3 shows the relevant topological features of this model, plotted for a subset of the state variables. An unstable periodic orbit, x^γ , separates solutions that fire periodic action potentials from those that converge towards a stable fixed point, x_0 . In panel A, two initial conditions are chosen on the unstable manifold of the unstable periodic orbit (dashed black line). The red line is in the basin of attraction of the stable periodic orbit. The blue line is in the basin of attraction of the stable fixed point. The slowest decaying eigenvalues of the fixed point are $\lambda_{1,2} = -0.035 \pm 0.461i$, with $\lambda_{3,4} = -0.473 \pm 0.408i$ being the next slowest. The slow eigenvalues λ_1 and λ_2 can be used to define the slow decaying isostable coordinate ψ_1 according to (7) with $\psi_2 = \psi_1^*$ and an associated slow manifold according to (27) with $\beta = 2$. As discussed in Section 3.1, this slow manifold is the intersection of the unstable manifold of the periodic orbit and the stable manifold of the fixed point. In panel A of Figure 3 the blue line is on the slow manifold of the stable fixed point. Blue and red lines in panel B of Figure 3 show the time course of V_1 for the blue and red trajectories shown in panel A. Panel C shows the transmembrane voltage of each neuron associated with the blue trajectory from panel A.

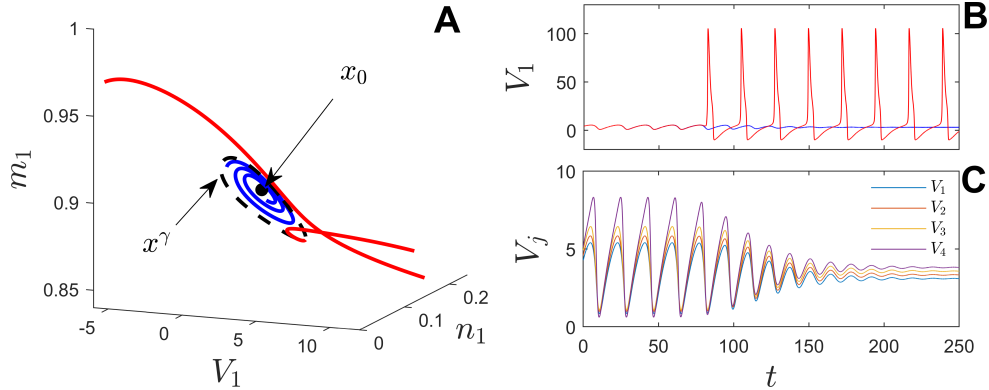


Figure 3: For the parameters used here, the model (63) is close to a subcritical Hopf bifurcation. An unstable periodic orbit, x^γ , separates solutions that decay to the stable fixed point x_0 and those that produce periodic action potentials. The blue line is on the slow manifold of the stable fixed point. Panel B shows V_1 for the blue and red trajectories from panel A over time. Panel C shows the transmembrane voltage of each neuron associated with the blue trajectory from panel A.

A set of initial conditions close to x^γ on its unstable manifold are integrated forward in time.

The resulting trajectories are used to trace out the slow manifold of the fixed point x_0 . ψ_1 is subsequently computed and level sets of $|\psi_1|$ are plotted as colored lines in panels A-D of Figure 4. For an initial condition in the basin of attraction of x_0 , the black line in Panels A-D show the evolution of V_j , n_j , and m_j for $j = 1, 2, 3, 4$ illustrating rapid convergence to the slow manifold. For this same initial condition, panel E shows the transmembrane voltage of each neuron over time. Despite having substantially different initial conditions, the plot quickly begins to resemble the plot from panel C of Figure 3, i.e., shown for a trajectory on the slow manifold.

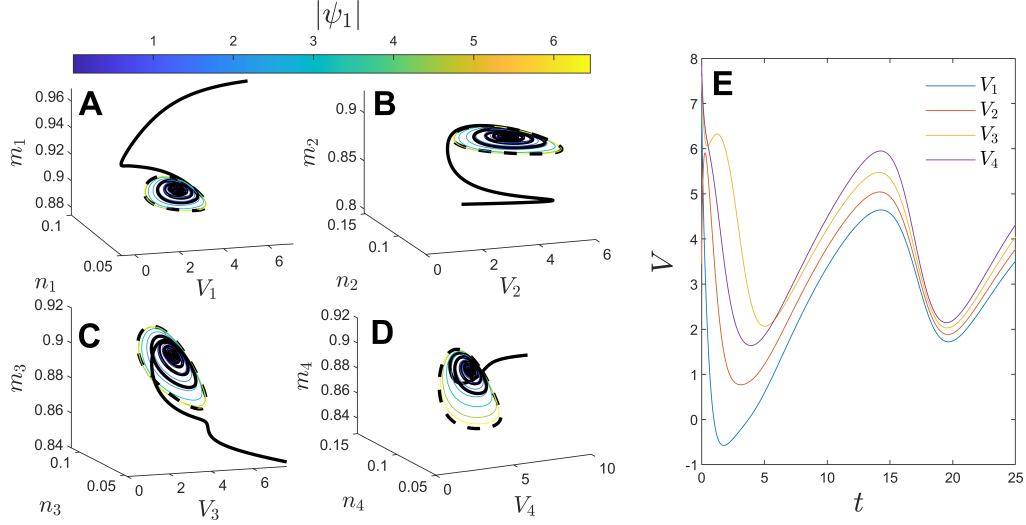


Figure 4: Level sets of $|\psi_1|$ on the slow manifold of x_0 are shown as colored lines in panels A-D. An initial condition in the basin of attraction of x_0 quickly converges to the slow manifold (black line). For the same trajectory, panel E shows voltage traces for each neuron for this trajectory.

The slow manifold of the fixed point x_0 can be used for model reduction by considering the evolution of the 16-dimensional model (63) on the 2-dimensional slow manifold. As an illustration of this point, we consider a control strategy designed to prevent (63) from firing an action potential in response to an external sine wave input. Let the input u be comprised of a sinusoidal forcing with an additional control input

$$u(t) = \zeta \sin(\omega_f t) + i(t), \quad (64)$$

where ζ and ω_f is the magnitude and frequency of the sinusoidal forcing, and $i(t)$ is an additional input that will be designed to control the state back to the basin of attraction of x_0 if the sinusoidal forcing causes it to leave. To implement such a control strategy, we focus on the dynamics of the isostable coordinates on the slow manifold. For an initial condition on the slow manifold, neglecting the faster decaying isostable coordinates, the slow isostable coordinate ψ_1 evolves according to a simplified version of (15)

$$\dot{\psi}_1 = \lambda_1 \psi_1 + I_\psi(\psi_1)u(t), \quad (65)$$

where $I_\psi(\psi_1) = \frac{\partial \psi_1}{\partial V_1} + \frac{\partial \psi_1}{\partial V_2}$ with partial derivatives evaluated at $x(\psi_1)$ (recall that input is only applied in the voltage equations of the first two neurons). Note that while there are two slow isostable coordinates, $\psi_1 = \psi_2^*$ so that I_ψ can be written as a function of only ψ_1 when restricted to the slow manifold. $I_1(\psi_1)$ can be obtained by first computing a set of trajectories on the slow manifold (for instance, the blue trajectory from panel A of Figure 3 could be one such trajectory),

computing I_1 along each trajectory using (16) and using the resulting information to interpolate $I_\psi(\psi)$ during simulations of (65). Equation (15) cannot be used to consider states beyond the basin of attraction of x_0 , however, since state approaches the unstable periodic orbit x^γ as $|\psi_1|$ approaches infinity. In order to consider states beyond the basin of attraction, once $|\psi_1|$ increases beyond some threshold, a phase reduction of the form (20) and (21) will be considered

$$\begin{aligned}\dot{\theta} &= \omega + z(\theta)u(t), \\ \dot{\hat{\psi}} &= \kappa\hat{\psi} + I_{\hat{\psi}}(\theta)u(t),\end{aligned}\tag{66}$$

where θ is the phase associated with the unstable periodic orbit, $\hat{\psi}$ is the isostable coordinate associated with its unstable Floquet multiplier $\kappa = 0.15$, and $\omega = 0.347$ rad/ms is the natural frequency. Once again, because input is only applied to the voltage equations of the first two neurons $z(\theta) = \frac{\partial \theta}{\partial V_1} + \frac{\partial \theta}{\partial V_2}$ and $I_{\hat{\psi}}(\theta) = \frac{\partial \hat{\psi}}{\partial V_1} + \frac{\partial \hat{\psi}}{\partial V_2}$ with partial derivatives evaluated at $x^\gamma(\theta)$. Note that Equation (66) is only valid for states close to the unstable periodic orbit, meaning that $\hat{\psi}$ must be small. In (66), $z(\theta)$ and $I_{\hat{\psi}}$ can be obtained by finding $Z(\theta)$ and $I_1(\theta)$ along $x^\gamma(t)$ using (22) and extracting the appropriate components.

The overall reduced order model for (63) is implemented as follows: Equation (65) is used when $|\psi_1| \leq 6$, i.e., when the state is far from the unstable periodic orbit. If $|\psi_1|$ becomes larger than 6, the state is close to x^γ and the state variables of (65) are converted to those of the phase reduction (66). For this reduction, $\hat{\psi} < 0$, corresponds to states in the basin of attraction of x_0 and $\hat{\psi} \geq 0$ are outside the basin of attraction. When $\hat{\psi}$ drops beyond a predetermined threshold, the state variables of (66) are converted back to those of isostable reduction (65). Having determined an appropriate reduced order model, a relatively simple control input for preventing action potentials is as follows: for an initial condition in the basin of attraction of x_0 , set the controller to be off so that $i(t) = 0$; when Equation (66) is active and $\hat{\psi} > \psi_{\text{on}}$, turn the controller on; when the controller is on let

$$i(t) = \begin{cases} -C\text{sign}(I_1(\psi_1)\psi_1^* + I_1^*(\psi_1)\psi_1), & \text{when Equation (65) is active,} \\ -C\text{sign}(I_0), & \text{when Equation (66) is active,} \end{cases}\tag{67}$$

where C is the applied control effort and $*$ denotes the complex conjugate; after the system returns to the basin of attraction and Equation (65) is active, if $|\psi_1| < \psi_{\text{off}}$, turn the controller off. The intuition behind the controller (67) is straightforward: when (66) is active, the controller drives $\hat{\psi}$ to smaller values to bring it back within the basin of attraction. When (65) is active, noticing that $\frac{d\psi_1}{dt}|\psi_1|^2 = \frac{d}{dt}(\psi_1\psi_1^*) = (\lambda_1 + \lambda_1^*)|\psi_1| + u(I_1(\psi_1)\psi_1^* + I_1^*(\psi_1)\psi_1)$, the controller drives $|\psi_1|$ to smaller values, bringing it further away from the boundary of the basin of attraction.

Figure 5 illustrates the aforementioned control strategy. In panel A, the shaded blue region represents the states that are handled with the reduction (65). It comprises most of the slow manifold, except for a small sliver near unstable periodic orbit (black dashed line). All other states are handled by the phase-amplitude reduction (66). For the sinusoidal input from (64), $\zeta = 1.1$ and $\omega_f = 0.57$. Over a 30 ms simulation, panel B shows the sine wave in black, along with the value of u as defined in (64) in red. The sudden drops in the applied control represent moments during which the controller is on, bringing the state back within the basin of attraction. The solid line in panel A show the trajectory in response to the applied input. It is colored red when the control is on and black when the control is off. Panel C shows a plot of V_1 over time for this simulation. The dashed line shows the same simulation when the control is off for the entire time (i.e., just the sine wave is applied) illustrating that the sinusoidal input causes an action potential. Panels D-G show the reduced order coordinates throughout the simulation. Panels D and E show $|\psi_1|$ and the argument of ψ_1 when Equation (65) is active. Panels F and G show representative plots of the

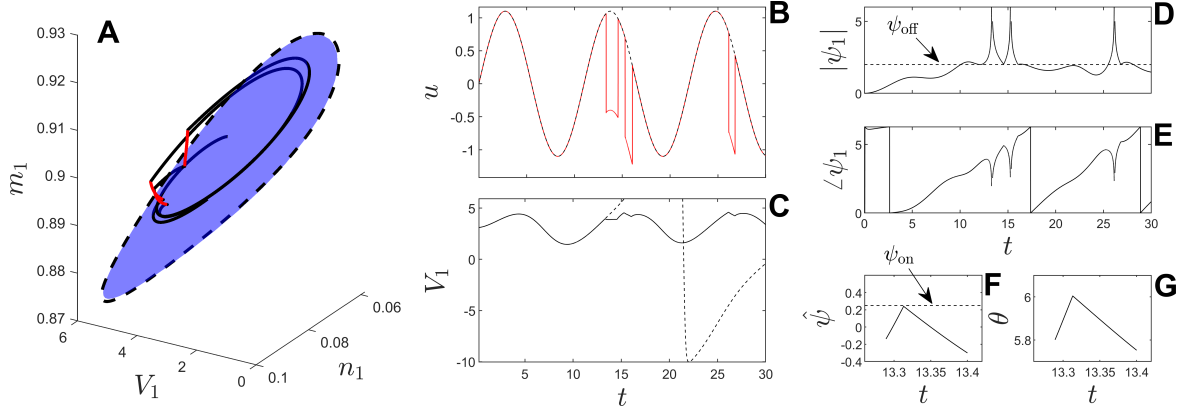


Figure 5: Illustration of a control strategy for preventing action potentials in the model (63) as described in the text. Panel A shows the slow manifold for a subset of the state variables as a blue surface. The unstable periodic orbit (dashed line) is the boundary of the basin of attraction on the slow manifold. The solid line shows the state in response to the control input. In panel B, a sine wave is shown in black. The red line shows $u(t)$ which differs from the sine wave when the control is active. Panel C provides a plot of V_1 during the course of the simulation. The dashed lines shows a comparison simulation taking $i(t) = 0$ (only the sine wave is applied) with a resulting action potential occurring at approximately $t = 20$. Panels D-G show the reduced order coordinates throughout the simulation with a detailed interpretation given in the text.

reduced order coordinates when (66) is active. Note that (65) and (66) are never simultaneously active which explains the gaps in each graph.

As an interpretation of the data in Panels D-G of Figure 5, for the first 13 milliseconds the state stays within the basin of attraction of the fixed point, and no control is applied. At approximately 13.29 seconds, the state approaches the unstable periodic orbit with $|\psi_1|$ increasing beyond the threshold to switch from (65) to (66). The sine wave input causes the state to exit the basin of attraction at approximately $\hat{\psi} = 13.3$ ms when $\hat{\psi} = 0$. Once $\hat{\psi}$ increases beyond $\psi_{\text{on}} = 0.25$, the controller turns on, driving the state back inside the basin of attraction. $\hat{\psi}$ decreasing below the threshold -0.3 prompts a switch from (66) to (65). The control remains on until approximately $t = 14.6$ ms when $|\psi_1|$ crosses $\psi_{\text{off}} = 2$. This process repeats throughout the remainder of the simulation, with the control turning on as necessary to prevent the system from firing an action potential. Note that for this simulation, the state is not prevented from leaving the basin of attraction of the fixed point, however, this could be mandated by setting $\psi_{\text{on}} = 0$ and rerunning the simulation.

4.2 Controlling an Oscillating Circadian Model to its Phaseless Set

Next, consider a 16 variable model (B1) that characterize the dynamical behavior of regulatory loops that govern the Per, Cry, Bmal1, and Clock genes [18] that give rise to circadian rhythms. Full model equations are provided in Appendix B. Time is in units of hours. An additive control input $u(t) \geq 0$ is applied to the M_B concentration dynamics. For the parameters used here, when $u(t) = 0$ this model has an unstable fixed point, x_0 , shown in Panel A of Figure 6 with unstable eigenvalues $\lambda_{1,2} = 0.0295 \pm 0.2776i$. An initial condition on the unstable manifold of x_0 converges to a stable periodic orbit x^γ in forward time. Panel A shows the evolution of such a trajectory, labeled $x(t)$. This periodic orbit has a natural frequency of 0.262 radians/hour with a period of

$T = 23.96$ hours. The slowest decaying isostable coordinates are $\kappa_1 = -0.029$, $\kappa_2 = -0.065$, and $\kappa_3 = -0.1238$. As compared to the example from Section 4.1 the gap between κ_1 and the faster Floquet exponents is not as pronounced. Nevertheless the slowest Floquet exponent κ_1 can still be used to define a slow decaying isostable coordinate ψ_1 according to (13) and an associated slow manifold on which $\psi_k = 0$ for $k \geq 2$.

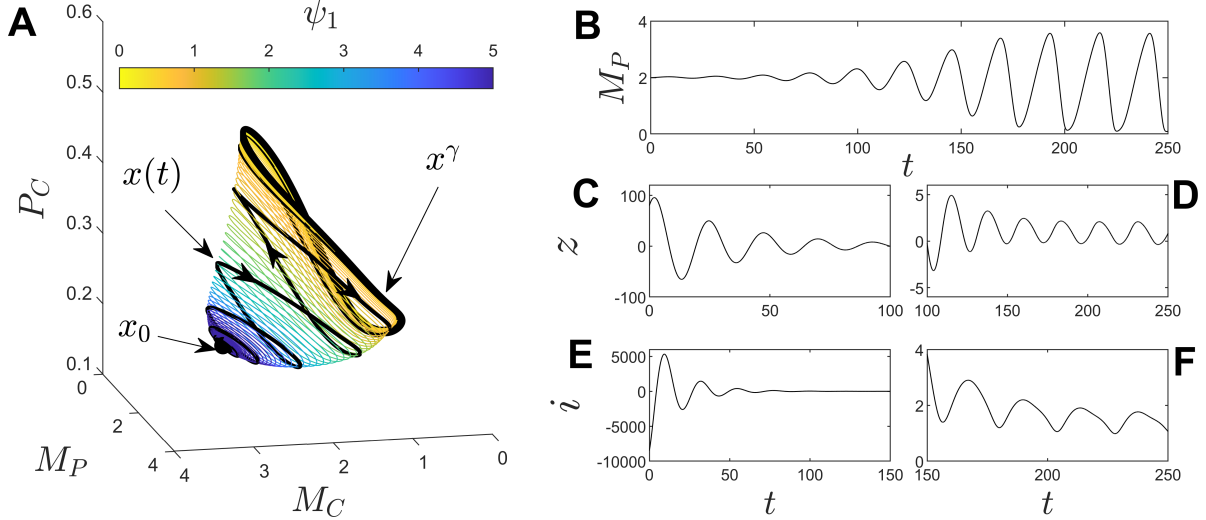


Figure 6: A slow manifold of (B1) is given by the intersection of the unstable manifold of the unstable fixed point, x_0 , and the stable manifold of the stable periodic orbit, x^γ . In panel A, the trajectory $x(t)$ is on this slow manifold, starting near x_0 and ending near x^γ . The colored lines show level sets of ψ_1 on the slow manifold. Panel B shows the variable M_P plotted along the trajectory $x(t)$. Recalling that an additive control input is added to M_P , Panels C-F show $z \equiv \frac{\partial \theta}{\partial M_P}$ and $i \equiv \frac{\partial \psi_1}{\partial M_P}$ plotted along the trajectory $x(t)$. These terms are relevant for reduced order modeling of the dynamics on the slow manifold.

As discussed in Section 3.3, the slow manifold for this system is the intersection of the unstable manifold of the fixed point and the stable manifold of the periodic orbit. A set of initial conditions close to x_0 on the unstable manifold are integrated forward in time and the resulting trajectories are used to trace out the slow manifold. Along these trajectories, gradients of the phase and isostable coordinates, Z and I_1 , respectively, are computed according to (22). Level sets of ψ_1 are plotted as colored lines in panel A of Figure 6. Panels B-F show relevant information associated with the trajectory $x(t)$. Panel B shows a trace of M_P , starting near the unstable fixed point and ending near the periodic orbit. Recall that the an additive control input is applied to the M_B dynamics; as such, for model reduction purposes $z \equiv \frac{\partial \theta}{\partial M_B}$ and $i \equiv \frac{\partial \psi_1}{\partial M_B}$ are the relevant curves. Panels C and D (resp. E and F) show z (resp., i) along the trajectory $x(t)$. Note that i is strictly positive in the latter portions of this trajectory (near the periodic orbit) but takes both positive and negative values in the earlier portions (near the fixed point). This feature will become important when discussing the control objective of driving the system from the periodic orbit to the unstable fixed point.

The slow manifold of the periodic orbit x^γ can be used for reduced order modeling by considering the evolution of the 16 dimensional model (B1) on the 2-dimensional slow manifold. The dynamics

of the phase and isostable coordinates on the slow manifold follow the general form (20) and (21)

$$\begin{aligned}\dot{\theta} &= \omega + z(\theta, \psi_1)u(t), \\ \dot{\psi}_1 &= \kappa_1 \psi_1 + i(\theta, \psi_1)u(t).\end{aligned}\tag{68}$$

Above, $z(\theta, \psi_1) = \frac{\partial \theta}{\partial M_P}$ and $i(\theta, \psi_1) = \frac{\partial \psi_1}{\partial M_P}$, where the partial derivatives are evaluated at $x(\theta, \psi_1)$ on the slow manifold. Both $z(\theta, \psi_1)$ and $i(\theta, \psi_1)$ can be computed by obtaining a set of trajectories on the slow manifold (for instance, the blue trajectory from panel A of Figure 6 could be one such trajectory), computing I_1 and Z along each trajectory using (22) and using the resulting information to interpolate z and i to perform simulations of (68).

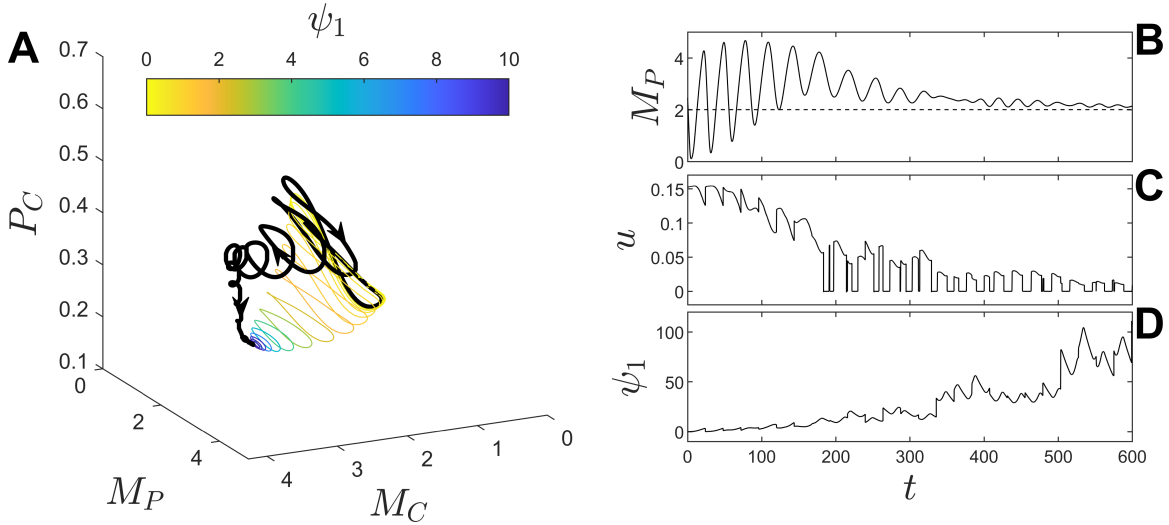


Figure 7: Applying the control strategy (69) to the circadian model (B1). In panel A, the controlled trajectory is plotted along side level sets of ψ_1 on the slow manifold. The slow manifold is not as strongly attracting as in the previous example, but nonetheless provides a reduced order representation that is accurate enough to achieve the control objective of driving the system to the unstable fixed point. Panels B, C, and D show M_P , u , and ψ_1 over time during this simulation. The value of ψ_1 from (68) is estimated and updated every T time units from measurements of $P_C(t)$ over the previous cycle.

The control objective for this example is to drive the state of (B1) from an initial condition on the periodic orbit to x_0 . For oscillatory systems, the fixed point is sometimes called the phaseless set, as all isochrons converge to this point [42], [26]. On the slow manifold, all trajectories converge to x_0 in the limit as ψ_1 approaches infinity. As such, using the reduced order model (68), driving the system from x^γ to x_0 is equivalent to increasing ψ_1 as much as possible after starting from $\psi_1 = 0$. From the level sets of ψ_1 in panel A of Figure 6, when $\psi_1 > 5$, the $x(\theta, \psi_1)$ is very close to x_0 . An additional constraint will be added requiring $u(t) \geq 0$ since it is generally easier to increase a given mRNA concentration (by adding more), than to decrease it. With the aforementioned points in mind, the specific control input used is

$$u(t) = \begin{cases} \frac{0.4\omega}{M(\psi_1)}, & \text{if } \text{sign}(i(\theta, \psi_1)) > 0, \\ 0, & \text{otherwise,} \end{cases}\tag{69}$$

where $M(\psi_1) = \max_{\theta}(|z(\theta, \psi_1)|)$. Intuitively, when $\text{sign}(i(\theta, \psi_1)) > 0$, a positive input is applied to drive the system to larger isostable coordinates (closer to x_0). The magnitude of the input is limited so that $z(\theta, \psi_1)u(t)$ cannot exceed 40 percent of ω and will shrink as the state gets closer to the target. Note that when applying this control strategy to the full equations (B1), θ and ψ_1 are not directly accessible. As such, the reduced order model (68) is simulated alongside (B1), with the values of $\theta(t)$ and $\psi_1(t)$ used to determine the applied control. Because (68) does not perfectly approximate the phase and isostable coordinates of the full order simulations, once every T units of simulation time, the amplitude and oscillation timing of $P_C(t)$ over the previous cycle is used to update θ and ψ_1 in (68). Figure 7 provides a representative example of this control strategy applied to the full model (B1). Panel C shows the applied input and panel D shows ψ_1 over the course of the simulation. Recall that ψ_1 is estimated from data every T time units which explains the vertical lines in panel D. Initially when the state is close to x^γ , u is positive which is consistent with the fact that $i(\theta, \psi_1) > 0$ when ψ_1 is near zero. Eventually as ψ_1 increases, $i(\theta, \psi_1) < 0$ in some places, which is consistent with the fact that $u = 0$ at some times as the simulation progresses. Panel A shows the trajectory during the simulation, superimposed on levels sets of ψ_1 for states on the slow manifold. Compared with the previous example from Section 4.1 the state does not converge as fast to the slow manifold due to smaller gap between κ_1 and κ_2 . Nonetheless, the reduced order model still enables a control strategy that can successfully achieve the control objective. Panel B shows M_p over time with the dashed horizontal line indicating the value of M_P at the unstable fixed point for reference.

For comparison, two additional control strategies are considered in Figure 8. For the first, instead of evaluating the gradients of the phase and amplitude coordinates on the slow manifold, they are evaluated only on the periodic orbit yielding a model of the form

$$\begin{aligned}\dot{\theta} &= \omega + z(\theta, 0)u(t), \\ \dot{\psi}_1 &= \kappa_1\psi_1 + i(\theta, 0)u(t).\end{aligned}\tag{70}$$

Equation (70) is similar to reduced order models used in [41], [25], [31]. While Equation (70) is generally easier to implement than (68) because it requires less information about the system, it is only valid in a close neighborhood of the periodic orbit. Using the reduced order model (70), a similar control strategy is applied to control the state of the full model to the unstable fixed point

$$u(t) = \begin{cases} \frac{0.4\omega}{M(0)}, & \text{if } \text{sign}(i(\theta, 0)) > 0, \\ 0, & \text{otherwise,} \end{cases}\tag{71}$$

with results shown in panels B D and E Figure 8. Panel E shows the applied control (red line) is constant in time, which is consistent with the fact that $i(\theta, \phi)$ is positive for all θ when $\phi = 0$. In panel B, the resulting trajectory is plotted along side level sets of ψ_1 on the slow manifold. As compared to the results from Figure 7 (shown in panel A for reference) the controlled trajectory is initially similar, but ultimately misses the target indicating that knowledge of the behavior on the entire slow manifold is necessary to successfully implement this control strategy.

A second control strategy based on a local linearization about x_0 is also considered. The linearized model takes the form

$$\Delta\dot{x} = A\Delta x + Bu(t),\tag{72}$$

where $\Delta x = x - x_0$, A is the Jacobian evaluated at x_0 , and $B \in \mathbb{R}^{16} = [0 \ 0 \ 1 \ 0 \ \dots \ 0]^T$ (recall that the input is added to the third variable). The unstable eigenvalues of the fixed point are $\lambda_{1,2} = 0.0295 \pm 0.2776i$. Let v_j and w_j be the left and right eigenvectors associated with the eigenvalue λ_j and let

$$y = [w_1 \ w_2]^T \Delta x \in \mathbb{C}^2,\tag{73}$$

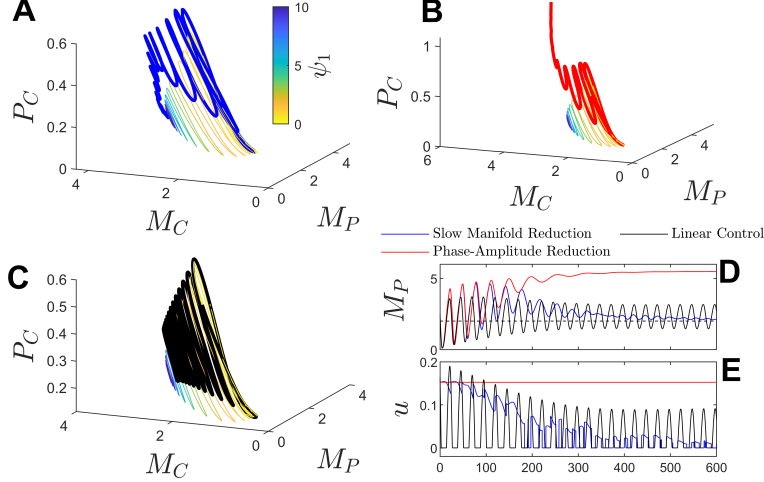


Figure 8: Comparison of two alternative control strategies for driving the state from the stable periodic orbit to the unstable fixed point (i.e., phaseless set). Panels A,D, and E show the same results from figure 7 for comparison. Panel B shows results when implementing a standard phase-amplitude reduction of the form (70). Panel C shows the results of the control (75) based on a linearization of the model equations. For each control strategy, panel D shows a plot of one M_P over time, with the horizontal dashed line being the value at the unstable fixed point. Panel E shows the control applied for each strategy. Both the linear control strategy and the standard phase-amplitude-based control strategy do not achieve the control objective, necessitating the use of (68) as the reduced order model for this example.

be the coordinates associated with the unstable eigenmodes. Changing variables, the dynamics of y follow

$$\dot{y} = \begin{bmatrix} \lambda_1 & 0 \\ 0 & \lambda_2 \end{bmatrix} y + \tilde{B}u(t), \quad (74)$$

where $\tilde{B} = [w_1 \ w_2]^T B$. A linear control strategy that is similar in spirit to (69) can then be designed with the goal of driving y to zero so that the system tends towards the fixed point. Noting that the components of $y = [y_1 \ y_2]^T$ are complex-conjugates, a simple control scheme designed to drive y_1 to lower magnitude values is

$$u(t) = \max(-\zeta[y_1^*(t)\tilde{B}_1 + y_1(t)\tilde{B}_1^*], 0), \quad (75)$$

where \tilde{B}_1 is the first entry of \tilde{B} , $*$ denotes the complex-conjugate, and ζ is a positive constant. The control (75) seeks to decrease the magnitude of $|\psi_1|$, with an input magnitude that decreases as the state approaches the fixed point. This linear control strategy (75) ignores the effect of stable eigenmodes, similar to the control using the slow manifold from (69). The linear control strategy (75) is applied to (B1), estimating the value of y according to (73) assuming direct access to all state variables. Results are shown in panels C-E of Figure 8 taking $\zeta = 0.08$. As seen in panel C, the state starts to tend towards x_0 but does not reach it, owing to unmodeled nonlinearities in the system. For the linear control strategy, larger values of ζ tend to destabilize the system, ultimately sending it far from the fixed point; smaller values of ζ yield steady state behavior with larger amplitude oscillations.

5 Conclusion

This work investigates the relationship between stable/unstable equilibria and their relationship to slow manifolds that are embedded in state space. As shown in Section 3, under appropriate technical conditions, a two-dimensional slow manifold as defined by (27) is given by the intersection of an unstable manifold of an unstable fixed point (resp., periodic orbit) and the stable manifold of a stable periodic orbit (resp., fixed point). This slow manifold can be approximated numerically by choosing a family of initial conditions near the unstable equilibrium, and integrating forward in time to provide a numerical approximation. The dynamics of isostable coordinates (and phase coordinate as appropriate) on the slow manifold can be considered via the transformation (15) when the fixed point is stable or via (20) and (21) when the periodic orbit is stable. These transformations ultimately yield a reduced order model that describes the behavior of the system near the slow manifold. Two biologically motivated systems are considered in this work to illustrate this reduced order modeling framework.

For the coupled population of Hodgkin-Huxley neurons considered in Section 4.1, the slow manifold defined according to (28) gives an estimate of the basin of attraction of the system's fixed point. Other Koopman-based strategies have been proposed for providing basin of attraction estimates for nonlinear dynamical systems [33], [20], but these methods would be difficult to scale to high dimensional systems due to either the use gridding the state space or due to the need to compute high order partial derivatives – the computational effort of both of these approaches increases exponentially with the dimension of the system. By contrast, restricting attention to a low-dimensional slow manifold allows one to circumvent issues caused by high dimensionality of the underlying system. The resulting reduced order model (65) in conjunction with the phase-based model (66) enables a simple control strategy that is able to drive the system state back to within the basin of attraction after escaping due to the influence of an external input.

For the circadian model considered in Section 4.2, the reduced order model giving the dynamics on the slow manifold allows for the design of a control algorithm to drive the state from a stable periodic orbit to an unstable fixed point (i.e., the phaseless set). As shown in the results from Figure 8, it is essential to understand the behavior along the entire slow manifold to achieve this control objective. Standard phase-based reduction methods and strategies based on local linearization do not contain sufficient information about the system dynamics control strategies based on these reductions do not achieve the control objective.

For a general system, in order to identify a slow manifold defined according to (28) and (29), it is first necessary to identify stable and unstable fixed points and periodic orbits present in a given dynamical system. This can pose a challenge, particularly in high dimensional dynamical systems, where the identification of unstable equilibria can be challenging. In this work, this computation is accomplished using bifurcation continuation techniques, starting, for instance from a stable fixed point and following the solution as a parameter is changed.

The proposed model order reduction techniques will not be applicable to all dynamical systems. Foremost, a sufficient timescale separation between the decay rates of the fast and slow isostable coordinates is necessary to obtain an accurate reduced order system. Larger timescale separation will produce more accurate reduced order models, however, moderate timescale difference can still yield accurate models (for instance, in Section 4.2 the slow Floquet exponent is $\kappa_1 = -0.029$ with the next slowest Floquet exponent being $\kappa_2 = -0.065$). For some systems, slow manifolds defined according to (27) do not approach an unstable fixed point or periodic orbit as time approaches negative infinity. For these systems, the slow manifold would need to be obtained using a different approach. Additionally, the results presented in this work are only applicable for systems with two-dimensional slow manifolds. Higher dimensional slow manifolds can be of interest, for instance,

to systems with multimodal nonlinear oscillations. Additional extensions to the current approach would be required to consider slow manifolds of higher dimension.

This material is based upon the work supported by the National Science Foundation (NSF) under Grant No. CMMI-2140527.

Appendix A Hodgkin-Huxley Model Equations

The dynamical model used in Section 4.1 consists of 4 coupled Hodgkin-Huxley neurons [11]. The equations are:

$$\begin{aligned} C_m \dot{V}_j &= -g_{\text{Na}} m_j^3 h_j (V_j - V_{\text{Na}}) - g_{\text{K}} n_j^4 (V_j - V_{\text{K}}) - g_{\text{L}} (V_j - V_{\text{L}}) - g_C (V_j - \bar{V}) + I_j + \alpha_j u(t), \\ \dot{n}_j &= \alpha_n (1 - n_j) - \beta_n n_j, \\ \dot{m}_j &= \alpha_m (1 - m_j) - \beta_m m_j, \\ \dot{h}_j &= \alpha_h (1 - h_j) - \beta_h h_j, \end{aligned} \tag{A1}$$

for $j = 1, \dots, 4$, where V_j is the transmembrane potential (in mV), and n_j , m_j , and $h_j \in [0, 1]$ are gating variables of the j^{th} neuron. $C_m = 1 \mu\text{F}/\text{cm}^2$ is the membrane capacitance, and $I_j = -4.318 + 0.75j \mu\text{A}/\text{cm}^2$ is the baseline current of each neuron. Coupling is electrotonic [12] with $g_C = 1.5$ and $\bar{V} = \frac{1}{4} \sum_{j=1}^4 V_j$. Here $u(t)$ is an input that represents a transmembrane current applied to only the first two neurons so that $\alpha_j = 1$ for $j = 1, 2$ and equals zero otherwise.

Maximal membrane conductances are

$$\begin{aligned} g_{\text{Na}} &= 120 \text{ mS}/\text{cm}^2, \\ g_{\text{K}} &= 36 \text{ mS}/\text{cm}^2, \\ g_{\text{L}} &= 1 \text{ mS}/\text{cm}^2, \end{aligned} \tag{A2}$$

and

$$\begin{aligned} V_{\text{Na}} &= 115 \text{ mV}, \\ V_{\text{K}} &= -12 \text{ mV}, \\ V_{\text{L}} &= 10.599 \text{ mV}, \end{aligned} \tag{A3}$$

are the reversal potentials of the associated ion channels. The rate constants are functions of the transmembrane voltage

$$\begin{aligned} \alpha_n &= 0.01(10 - V)/(\exp((10 - V)/10) - 1), \\ \beta_n &= 0.125 \exp(-V/80), \\ \alpha_m &= 0.1(25 - V)/(\exp((25 - V)/10) - 1), \\ \beta_m &= 4 \exp(-V/18), \\ \alpha_h &= 0.7 \exp(-V/20), \\ \beta_h &= 1/(\exp((-V + 30)/10) + 1). \end{aligned} \tag{A4}$$

Appendix B Circadian Model Equations

The circadian oscillator model used in Section 4.2 was published in [18]. The version used here has 16 coupled ordinary differential equations. The state variables are as follows: concentrations

of Per, Cry, and Bmal1 mRNA are designated by M_P , M_C , and M_B , respectively; phosphorylated (resp., nonphosphorylated) Per and Cry proteins in cytosol are designated by P_{CP} and C_{CP} (resp., P_C and C_C); concentrations of Per-Cry complex in cytosol and nucleus are designated by PC_C , PC_N , PC_{CP} , and PC_{NP} ; concentrations of BMAL1 in cytosol and nucleus are designated by B_C , B_{CP} , B_N , and B_{NP} ; Inactive complex between Per-Cry and Clock-Bmal1 in the nucleus is designated by I_N . Subscripts C , N , CP and NP denote cytosolic, nuclear, cytosolic phosphorylated, and nuclear phosphorylated forms, respectively. The model equations are:

$$\begin{aligned}
\dot{M}_P &= v_{sP} \frac{B_N^n}{K_{AP}^n + B_N^n} - v_{mP} \frac{M_P}{K_{mP} + M_P} - k_{dmp} M_P, \\
\dot{M}_C &= v_{sC} \frac{B_N^n}{K_{AC}^n + B_N^n} - v_{mC} \frac{M_C}{K_{mC} + M_C} - k_{dmc} M_C, \\
\dot{M}_B &= v_{sB} \frac{K_{IB}^m}{K_{IB}^m + B_N^m} - v_{mB} \frac{M_B}{K_{mB} + M_B} - k_{dmb} M_B + u(t), \\
\dot{P}_C &= k_{sP} M_P - V_{1P} \frac{P_C}{K_p + P_C} + V_{2P} \frac{P_{CP}}{K_{dp} + P_{CP}} + k_4 PC_C - k_3 P_C C_C - k_{dn} P_C, \\
\dot{C}_C &= k_{sC} M_C - V_{1C} \frac{C_C}{K_p + C_C} + V_{2C} \frac{C_{CP}}{K_{dp} + C_{CP}} + k_4 PC_C - k_3 P_C C_C - k_{dnc} C_C, \\
\dot{P}_{CP} &= V_{1P} \frac{P_C}{K_p + P_C} - V_{2P} \frac{P_{CP}}{K_{dp} + P_{CP}} - v_{dPC} \frac{P_{CP}}{K_d + P_{CP}} - k_{dn} P_{CP}, \\
\dot{C}_{CP} &= V_{1C} \frac{C_C}{K_p + C_C} - V_{2C} \frac{C_{CP}}{K_{dp} + C_{CP}} - v_{dCC} \frac{C_{CP}}{K_d + C_{CP}} - k_{dn} C_{CP}, \\
\dot{P}C_C &= -V_{1PC} \frac{PC_C}{K_p + PC_C} + V_{2PC} \frac{PC_{CP}}{K_{dp} + PC_{CP}} - k_4 PC_C + k_3 P_C C_C \\
&\quad + k_2 PC_N - k_1 PC_C - k_{dn} PC_C, \\
\dot{P}C_N &= -V_{3PC} \frac{PC_N}{K_p + PC_N} + V_{4PC} \frac{PC_{NP}}{K_{dp} + PC_{NP}} - k_2 PC_N + k_1 PC_C \\
&\quad - k_7 B_N PC_N + k_8 I_N - k_{dn} PC_N, \\
\dot{P}C_{CP} &= V_{1PC} \frac{PC_C}{K_p + PC_C} - V_{2PC} \frac{PC_{CP}}{K_{dp} + PC_{CP}} - v_{dPCC} \frac{PC_{CP}}{K_d + PC_{CP}} - k_{dn} PC_{CP}, \\
\dot{P}C_{NP} &= -V_{3PC} \frac{PC_N}{K_p + PC_N} - V_{4PC} \frac{PC_{NP}}{K_{dp} + PC_{NP}} - v_{dPCN} \frac{PC_{NP}}{K_d + PC_{NP}} - k_{dn} PC_{NP}, \\
\dot{B}_C &= k_{sB} M_B - V_{1B} \frac{B_C}{K_p + B_C} + V_{2B} \frac{B_{CP}}{K_{dp} + B_{CP}} - k_5 B_C + k_6 B_N - k_{dn} B_C, \\
\dot{B}_{CP} &= V_{1B} \frac{B_C}{K_p + B_C} - V_{2B} \frac{B_{CP}}{K_{dp} + B_{CP}} - v_{dBC} \frac{B_{CP}}{K_d + B_{CP}} - k_{dn} B_{CP}, \\
\dot{B}_N &= -V_{3B} \frac{B_N}{K_p + B_N} + V_{4B} \frac{B_{NP}}{K_{dp} + B_{NP}} + k_5 B_C - k_6 B_N - k_7 B_N PC_N \\
&\quad + k_8 I_N - k_{dn} B_N, \\
\dot{B}_{NP} &= V_{3B} \frac{B_N}{K_p + B_N} - V_{4B} \frac{B_{NP}}{K_{dp} + B_{NP}} - v_{dBN} \frac{B_{NP}}{K_d + B_{NP}} - k_{dn} B_{NP}, \\
\dot{I}_N &= -k_8 I_N + k_7 B_N PC_N - v_{dIN} \frac{I_N}{K_d + I_N} - k_{dn} I_N.
\end{aligned} \tag{B1}$$

Basal values listed in Supplementary Table 1 of [18] are used with the exception of $k_1 = 0.58$ and $k_2 = 2.0$, which determine the dynamics of the nonphosphorylated Per-Cry complex. Units of time are in hours. The light intensity impacts the maximum rate of Per expression and is taken to be $v_{sP} = 1.35$. A control input $u(t)$ is added to the M_B concentration dynamics.

References

- [1] T. Ahmed, A. Sadovnik, and D. Wilson. Data-driven inference of low-order isostable-coordinate-based dynamical models using neural networks. *Nonlinear Dynamics*, 111(3):2501–2519, 2023.
- [2] S. L. Brunton, B. W. Brunton, J. L. Proctor, and J. N. Kutz. Koopman invariant subspaces and finite linear representations of nonlinear dynamical systems for control. *PloS One*, 11(2), 2016.
- [3] M. Cenedese, J. Axås, B. Bäuerlein, K. Avila, and G. Haller. Data-driven modeling and prediction of non-linearizable dynamics via spectral submanifolds. *Nature Communications*, 13(1):872, 2022.
- [4] S. Farjami, V. Kirk, and H. M. Osinga. Computing the stable manifold of a saddle slow manifold. *SIAM Journal on Applied Dynamical Systems*, 17(1):350–379, 2018.
- [5] N. Fenichel. Geometric singular perturbation theory for ordinary differential equations. *Journal of differential equations*, 31(1):53–98, 1979.
- [6] C. Foias, M. S. Jolly, I. G. Kevrekidis, G. R. Sell, and E. S. Titi. On the computation of inertial manifolds. *Physics Letters A*, 131(7):433–436, 1988.
- [7] C. Foias, G. R. Sell, and R. Temam. Inertial manifolds for nonlinear evolutionary equations. *Journal of Differential Equations*, 73(2):309–353, 1988.
- [8] J. Guckenheimer. Isochrons and phaseless sets. *Journal of Mathematical Biology*, 1(3):259–273, 1975.
- [9] J. Guckenheimer and C. Kuehn. Computing slow manifolds of saddle type. *SIAM Journal on Applied Dynamical Systems*, 8(3):854–879, 2009.
- [10] G. Haller and S. Ponsioen. Nonlinear normal modes and spectral submanifolds: existence, uniqueness and use in model reduction. *Nonlinear Dynamics*, 86:1493–1534, 2016.
- [11] A. L. Hodgkin and A. F. Huxley. A quantitative description of membrane current and its application to conduction and excitation in nerve. *J. Physiol.*, 117:500–44, 1952.
- [12] D. Johnston and S. M.-S. Wu. *Foundations of Cellular Neurophysiology*. MIT Press, Cambridge, MA, 1995.
- [13] D. Jordan and P. Smith. *Nonlinear Ordinary Differential Equations: An Introduction for Scientists and Engineers*, volume 10. Oxford University Press, Oxford, 2007.
- [14] E. Kaiser, J. N. Kutz, and S. Brunton. Data-driven discovery of Koopman eigenfunctions for control. *Machine Learning: Science and Technology*, 2021.

- [15] T. J. Kaper. Systems theory for singular perturbation problems. In *Analyzing multiscale phenomena using singular perturbation methods*, pages 85–131. AMS, 1999.
- [16] J. N. Kutz, S. L. Brunton, B. W. Brunton, and J. L. Proctor. *Dynamic mode decomposition: data-driven modeling of complex systems*. Society for Industrial and Applied Mathematics, Philadelphia, PA, 2016.
- [17] M. D. Kvalheim and S. Revzen. Existence and uniqueness of global Koopman eigenfunctions for stable fixed points and periodic orbits. *Physica D: Nonlinear Phenomena*, page 132959, 2021.
- [18] J. C. Leloup and A. Goldbeter. Toward a detailed computational model for the mammalian circadian clock. *Proceedings of the National Academy of Sciences*, 100(12):7051–7056, 2003.
- [19] B. Lusch, J. N. Kutz, and S. L. Brunton. Deep learning for universal linear embeddings of nonlinear dynamics. *Nature Communications*, 9(1):1–10, 2018.
- [20] A. Mauroy and I. Mezić. Global stability analysis using the eigenfunctions of the Koopman operator. *IEEE Transactions on Automatic Control*, 61(11):3356–3369, 2016.
- [21] A. Mauroy, I. Mezić, and J. Moehlis. Isostables, isochrons, and Koopman spectrum for the action–angle representation of stable fixed point dynamics. *Physica D: Nonlinear Phenomena*, 261:19–30, 2013.
- [22] I. Mezić. Analysis of fluid flows via spectral properties of the Koopman operator. *Annual Review of Fluid Mechanics*, 45:357–378, 2013.
- [23] I. Mezić. Spectrum of the Koopman operator, spectral expansions in functional spaces, and state-space geometry. *Journal of Nonlinear Science*, pages 1–55, 2019.
- [24] I. Mezić. Spectrum of the Koopman operator, spectral expansions in functional spaces, and state-space geometry. *Journal of Nonlinear Science*, 30(5):2091–2145, 2020.
- [25] B. Monga and J. Moehlis. Optimal phase control of biological oscillators using augmented phase reduction. *Biological Cybernetics*, 113(1-2):161–178, 2019.
- [26] H. M. Osinga and J. Moehlis. Continuation-based computation of global isochrons. *SIAM Journal on Applied Dynamical Systems*, 9(4):1201–1228, 2010.
- [27] Y. Park and D. Wilson. -body oscillator interactions of higher-order coupling functions. *SIAM Journal on Applied Dynamical Systems*, 23(2):1471–1503, 2024.
- [28] S. Ponsioen, S. Jain, and G. Haller. Model reduction to spectral submanifolds and forced-response calculation in high-dimensional mechanical systems. *Journal of Sound and Vibration*, 488:115640, 2020.
- [29] P. J. Schmid. Dynamic mode decomposition of numerical and experimental data. *Journal of Fluid Mechanics*, 656:5–28, 2010.
- [30] A. Sootla and A. Mauroy. Geometric properties of isostables and basins of attraction of monotone systems. *IEEE Transactions on Automatic Control*, 62(12):6183–6194, 2017.

- [31] S. Takata, Y. Kato, and H. Nakao. Fast optimal entrainment of limit-cycle oscillators by strong periodic inputs via phase-amplitude reduction and Floquet theory. *Chaos: An Interdisciplinary Journal of Nonlinear Science*, 31(9), 2021.
- [32] S. Wiggins. *Introduction to applied nonlinear dynamical systems and chaos*, volume 2. Springer, 2003.
- [33] M. O. Williams, I. G. Kevrekidis, and C. W. Rowley. A data-driven approximation of the koopman operator: Extending dynamic mode decomposition. *Journal of Nonlinear Science*, 25(6):1307–1346, 2015.
- [34] D. Wilson. A data-driven phase and isostable reduced modeling framework for oscillatory dynamical systems. *Chaos: An Interdisciplinary Journal of Nonlinear Science*, 30(1):013121, 2020.
- [35] D. Wilson. Phase-amplitude reduction far beyond the weakly perturbed paradigm. *Physical Review E*, 101(2):022220, 2020.
- [36] D. Wilson. Identification and computation of slow manifolds using the isostable coordinate system. *arXiv preprint:PENDING*, 202025.
- [37] D. Wilson. Analysis of input-induced oscillations using the isostable coordinate framework. *Chaos: An Interdisciplinary Journal of Nonlinear Science*, 31(2):023131, 2021.
- [38] D. Wilson. Data-driven inference of high-accuracy isostable-based dynamical models in response to external inputs. *Chaos: An Interdisciplinary Journal of Nonlinear Science*, 31(6):063137, 2021.
- [39] D. Wilson. An adaptive phase-amplitude reduction framework without $\mathcal{O}(\epsilon)$ constraints on inputs. *SIAM Journal on Applied Dynamical Systems*, 21(1):204–230, 2022.
- [40] D. Wilson and B. Ermentrout. Greater accuracy and broadened applicability of phase reduction using isostable coordinates. *Journal of Mathematical Biology*, 76(1-2):37–66, 2018.
- [41] D. Wilson and J. Moehlis. Isostable reduction of periodic orbits. *Physical Review E*, 94(5):052213, 2016.
- [42] A. Winfree. *The Geometry of Biological Time*. Springer Verlag, New York, second edition, 2001.